

Amplitude analysis and branching fraction measurement of the decay $D_s^+ \rightarrow \pi^+ \pi^0 \pi^0$

BESIII Collaboration



M. Ablikim¹, M. N. Achasov^{10,b}, P. Adlarson⁶⁶, S. Ahmed¹⁴, M. Albrecht⁴,
 R. Aliberti²⁷, A. Amoroso^{65A,65C}, M. R. An³¹, Q. An^{62,48}, X. H. Bai⁵⁶, Y. Bai⁴⁷,
 O. Bakina²⁸, R. Baldini Ferroli^{22A}, I. Balossino^{23A}, Y. Ban^{37,h}, K. Begzsuren²⁵,
 N. Berger²⁷, M. Bertani^{22A}, D. Bettoni^{23A}, F. Bianchi^{65A,65C}, J. Bloms⁵⁹,
 A. Bortone^{65A,65C}, I. Boyko²⁸, R. A. Briere⁵, H. Cai⁶⁷, X. Cai^{1,48}, A. Calcaterra^{22A},
 G. F. Cao^{1,53}, N. Cao^{1,53}, S. A. Cetin^{52A}, J. F. Chang^{1,48}, W. L. Chang^{1,53},
 G. Chelkov^{28,a}, D. Y. Chen⁶, G. Chen¹, H. S. Chen^{1,53}, M. L. Chen^{1,48}, S. J. Chen³⁴,
 X. R. Chen²⁴, Y. B. Chen^{1,48}, Z. J. Chen^{19,i}, W. S. Cheng^{65C}, G. Cibinetto^{23A},
 F. Cossio^{65C}, X. F. Cui³⁵, H. L. Dai^{1,48}, X. C. Dai^{1,53}, A. Dbeyssi¹⁴, R. E. de Boer⁴,
 D. Dedovich²⁸, Z. Y. Deng¹, A. Denig²⁷, I. Denysenko²⁸, M. Destefanis^{65A,65C},
 F. De Mori^{65A,65C}, Y. Ding³², C. Dong³⁵, J. Dong^{1,48}, L. Y. Dong^{1,53},
 M. Y. Dong^{1,48,53}, X. Dong⁶⁷, S. X. Du⁷⁰, Y. L. Fan⁶⁷, J. Fang^{1,48}, S. S. Fang^{1,53},
 Y. Fang¹, R. Farinelli^{23A}, L. Fava^{65B,65C}, F. Feldbauer⁴, G. Felici^{22A}, C. Q. Feng^{62,48},
 J. H. Feng⁴⁹, M. Fritsch⁴, C. D. Fu¹, Y. Gao⁶³, Y. Gao^{62,48}, Y. Gao^{37,h}, Y. G. Gao⁶,
 I. Garzia^{23A,23B}, P. T. Ge⁶⁷, C. Geng⁴⁹, E. M. Gersabeck⁵⁷, A. Gilman⁶⁰, K. Goetzen¹¹,
 L. Gong³², W. X. Gong^{1,48}, W. Gradl²⁷, M. Greco^{65A,65C}, L. M. Gu³⁴, M. H. Gu^{1,48},
 C. Y. Guan^{1,53}, A. Q. Guo²¹, L. B. Guo³³, R. P. Guo³⁹, Y. P. Guo^{9,f}, A. Guskov^{28,a},
 T. T. Han⁴⁰, W. Y. Han³¹, X. Q. Hao¹⁵, F. A. Harris⁵⁵, K. L. He^{1,53}, F. H. Heinsius⁴,
 C. H. Heinz²⁷, T. Held⁴, Y. K. Heng^{1,48,53}, C. Herold⁵⁰, M. Himmelreich^{11,d},
 T. Holtmann⁴, G. Y. Hou^{1,53}, Y. R. Hou⁵³, Z. L. Hou¹, H. M. Hu^{1,53}, J. F. Hu^{46,j},
 T. Hu^{1,48,53}, Y. Hu¹, G. S. Huang^{62,48}, L. Q. Huang⁶³, X. T. Huang⁴⁰, Y. P. Huang¹,
 Z. Huang^{37,h}, T. Hussain⁶⁴, N. Hüsken^{21,27}, W. Ikegami Andersson⁶⁶, W. Imoehl²¹,
 M. Irshad^{62,48}, S. Jaeger⁴, S. Janchiv²⁵, Q. Ji¹, Q. P. Ji¹⁵, X. B. Ji^{1,53}, X. L. Ji^{1,48},
 Y. Y. Ji⁴⁰, H. B. Jiang⁴⁰, X. S. Jiang^{1,48,53}, J. B. Jiao⁴⁰, Z. Jiao¹⁷, S. Jin³⁴, Y. Jin⁵⁶,
 M. Q. Jing^{1,53}, T. Johansson⁶⁶, N. Kalantar-Nayestanaki⁵⁴, X. S. Kang³²,
 R. Kappert⁵⁴, M. Kavatsyuk⁵⁴, B. C. Ke^{70,42}, I. K. Keshk⁴, A. Khoukaz⁵⁹, P. Kiese²⁷,
 R. Kiuchi¹, R. Kliemt¹¹, L. Koch²⁹, O. B. Kolcu^{52A,m}, B. Kopf⁴, M. Kuemmel⁴,
 M. Kuessner⁴, A. Kupsc⁶⁶, M. G. Kurth^{1,53}, W. Kühn²⁹, J. J. Lane⁵⁷, J. S. Lange²⁹,

P. Larin¹⁴, A. Lavania²⁰, L. Lavezzi^{65A,65C}, Z. H. Lei^{62,48}, H. Leithoff²⁷,
 M. Lellmann²⁷, T. Lenz²⁷, C. Li³⁸, C. H. Li³¹, Cheng Li^{62,48}, D. M. Li⁷⁰, F. Li^{1,48},
 G. Li¹, H. Li⁴², H. Li^{62,48}, H. B. Li^{1,53}, H. J. Li¹⁵, J. L. Li⁴⁰, J. Q. Li⁴, J. S. Li⁴⁹,
 Ke Li¹, L. K. Li¹, Lei Li³, P. R. Li^{30,k,l}, S. Y. Li⁵¹, W. D. Li^{1,53}, W. G. Li¹,
 X. H. Li^{62,48}, X. L. Li⁴⁰, Xiaoyu Li^{1,53}, Z. Y. Li⁴⁹, H. Liang^{62,48}, H. Liang^{1,53},
 H. Liang²⁶, Y. F. Liang⁴⁴, Y. T. Liang²⁴, G. R. Liao¹², L. Z. Liao^{1,53}, J. Libby²⁰,
 C. X. Lin⁴⁹, T. Lin¹, B. J. Liu¹, C. X. Liu¹, D. Liu^{14,62}, F. H. Liu⁴³, Fang Liu¹,
 Feng Liu⁶, H. M. Liu^{1,53}, Huanhuan Liu¹, Huihui Liu¹⁶, J. B. Liu^{62,48}, J. L. Liu⁶³,
 J. Y. Liu^{1,53}, K. Liu¹, K. Y. Liu³², L. Liu^{62,48}, M. H. Liu^{9,f}, P. L. Liu¹, Q. Liu⁶⁷,
 Q. Liu⁵³, S. B. Liu^{62,48}, Shuai Liu⁴⁵, T. Liu^{1,53}, W. M. Liu^{62,48}, X. Liu^{30,k,l}, Y. Liu^{30,k,l},
 Y. B. Liu³⁵, Z. A. Liu^{1,48,53}, Z. Q. Liu⁴⁰, X. C. Lou^{1,48,53}, F. X. Lu⁴⁹, H. J. Lu¹⁷,
 J. D. Lu^{1,53}, J. G. Lu^{1,48}, X. L. Lu¹, Y. Lu¹, Y. P. Lu^{1,48}, C. L. Luo³³, M. X. Luo⁶⁹,
 P. W. Luo⁴⁹, T. Luo^{9,f}, X. L. Luo^{1,48}, X. R. Lyu⁵³, F. C. Ma³², H. L. Ma¹, L. L. Ma⁴⁰,
 M. M. Ma^{1,53}, Q. M. Ma¹, R. Q. Ma^{1,53}, R. T. Ma⁵³, X. X. Ma^{1,53}, X. Y. Ma^{1,48},
 F. E. Maas¹⁴, M. Maggiora^{65A,65C}, S. Maldaner⁴, S. Malde⁶⁰, Q. A. Malik⁶⁴,
 A. Mangoni^{22B}, Y. J. Mao^{37,h}, Z. P. Mao¹, S. Marcello^{65A,65C}, Z. X. Meng⁵⁶,
 J. G. Messchendorp⁵⁴, G. Mezzadri^{23A}, T. J. Min³⁴, R. E. Mitchell²¹, X. H. Mo^{1,48,53},
 N. Yu. Muchnoi^{10,b}, H. Muramatsu⁵⁸, S. Nakhoul^{11,d}, Y. Nefedov²⁸, F. Nerling^{11,d},
 I. B. Nikolaev^{10,b}, Z. Ning^{1,48}, S. Nisar^{8,g}, Q. Ouyang^{1,48,53}, S. Pacetti^{22B,22C},
 X. Pan^{9,f}, Y. Pan⁵⁷, A. Pathak¹, A. Pathak²⁶, P. Patteri^{22A}, M. Pelizaeus⁴,
 H. P. Peng^{62,48}, K. Peters^{11,d}, J. Pettersson⁶⁶, J. L. Ping³³, R. G. Ping^{1,53},
 S. Pogodin²⁸, R. Poling⁵⁸, V. Prasad^{62,48}, H. Qi^{62,48}, H. R. Qi⁵¹, K. H. Qi²⁴, M. Qi³⁴,
 T. Y. Qi⁹, S. Qian^{1,48}, W. B. Qian⁵³, Z. Qian⁴⁹, C. F. Qiao⁵³, L. Q. Qin¹², X. P. Qin⁹,
 X. S. Qin⁴⁰, Z. H. Qin^{1,48}, J. F. Qiu¹, S. Q. Qu³⁵, K. H. Rashid⁶⁴, K. Ravindran²⁰,
 C. F. Redmer²⁷, A. Rivetti^{65C}, V. Rodin⁵⁴, M. Rolo^{65C}, G. Rong^{1,53}, Ch. Rosner¹⁴,
 M. Rump⁵⁹, H. S. Sang⁶², A. Sarantsev^{28,c}, Y. Schelhaas²⁷, C. Schnier⁴,
 K. Schoenning⁶⁶, M. Scodreggio^{23A,23B}, D. C. Shan⁴⁵, W. Shan¹⁸, X. Y. Shan^{62,48},
 J. F. Shangguan⁴⁵, M. Shao^{62,48}, C. P. Shen⁹, H. F. Shen^{1,53}, P. X. Shen³⁵,
 X. Y. Shen^{1,53}, H. C. Shi^{62,48}, R. S. Shi^{1,53}, X. Shi^{1,48}, X. D. Shi^{62,48}, J. J. Song⁴⁰,
 W. M. Song^{26,1}, Y. X. Song^{37,h}, S. Sosio^{65A,65C}, S. Spataro^{65A,65C}, K. X. Su⁶⁷,
 P. P. Su⁴⁵, F. F. Sui⁴⁰, G. X. Sun¹, H. K. Sun¹, J. F. Sun¹⁵, L. Sun⁶⁷, S. S. Sun^{1,53},
 T. Sun^{1,53}, W. Y. Sun³³, W. Y. Sun²⁶, X. Sun^{19,i}, Y. J. Sun^{62,48}, Y. Z. Sun¹,
 Z. T. Sun¹, Y. H. Tan⁶⁷, Y. X. Tan^{62,48}, C. J. Tang⁴⁴, G. Y. Tang¹, J. Tang⁴⁹,
 J. X. Teng^{62,48}, V. Thoren⁶⁶, W. H. Tian⁴², Y. T. Tian²⁴, I. Uman^{52B}, B. Wang¹,
 C. W. Wang³⁴, D. Y. Wang^{37,h}, H. J. Wang^{30,k,l}, H. P. Wang^{1,53}, K. Wang^{1,48},
 L. L. Wang¹, M. Wang⁴⁰, M. Z. Wang^{37,h}, Meng Wang^{1,53}, S. Wang^{9,f}, W. Wang⁴⁹,
 W. H. Wang⁶⁷, W. P. Wang^{62,48}, X. Wang^{37,h}, X. F. Wang^{30,k,l}, X. L. Wang^{9,f},
 Y. Wang⁴⁹, Y. Wang^{62,48}, Y. D. Wang³⁶, Y. F. Wang^{1,48,53}, Y. Q. Wang¹,
 Y. Y. Wang^{30,k,l}, Z. Wang^{1,48}, Z. Y. Wang¹, Ziyi Wang⁵³, Zongyuan Wang^{1,53},
 D. H. Wei¹², F. Weidner⁵⁹, S. P. Wen¹, D. J. White⁵⁷, U. Wiedner⁴, G. Wilkinson⁶⁰,
 M. Wolke⁶⁶, L. Wollenberg⁴, J. F. Wu^{1,53}, L. H. Wu¹, L. J. Wu^{1,53}, X. Wu^{9,f},
 Z. Wu^{1,48}, L. Xia^{62,48}, H. Xiao^{9,f}, S. Y. Xiao¹, Z. J. Xiao³³, X. H. Xie^{37,h},
 Y. G. Xie^{1,48}, Y. H. Xie⁶, T. Y. Xing^{1,53}, G. F. Xu¹, Q. J. Xu¹³, W. Xu^{1,53},

X. P. Xu⁴⁵, Y. C. Xu⁵³, F. Yan^{9,f}, L. Yan^{9,f}, W. B. Yan^{62,48}, W. C. Yan⁷⁰, Xu Yan⁴⁵, H. J. Yang^{41,e}, H. X. Yang¹, L. Yang⁴², S. L. Yang⁵³, Y. X. Yang¹², Yifan Yang^{1,53}, Zhi Yang²⁴, M. Ye^{1,48}, M. H. Ye⁷, J. H. Yin¹, Z. Y. You⁴⁹, B. X. Yu^{1,48,53}, C. X. Yu³⁵, G. Yu^{1,53}, J. S. Yu^{19,i}, T. Yu⁶³, C. Z. Yuan^{1,53}, L. Yuan², X. Q. Yuan^{37,h}, Y. Yuan¹, Z. Y. Yuan⁴⁹, C. X. Yue³¹, A. A. Zafar⁶⁴, X. Zeng Zeng⁶, Y. Zeng^{19,i}, A. Q. Zhang¹, B. X. Zhang¹, Guangyi Zhang¹⁵, H. Zhang⁶², H. H. Zhang⁴⁹, H. H. Zhang²⁶, H. Y. Zhang^{1,48}, J. J. Zhang⁴², J. L. Zhang⁶⁸, J. Q. Zhang³³, J. W. Zhang^{1,48,53}, J. Y. Zhang¹, J. Z. Zhang^{1,53}, Jianyu Zhang^{1,53}, Jiawei Zhang^{1,53}, L. M. Zhang⁵¹, L. Q. Zhang⁴⁹, Lei Zhang³⁴, S. Zhang⁴⁹, S. F. Zhang³⁴, Shulei Zhang^{19,i}, X. D. Zhang³⁶, X. Y. Zhang⁴⁰, Y. Zhang⁶⁰, Y. T. Zhang⁷⁰, Y. H. Zhang^{1,48}, Yan Zhang^{62,48}, Yao Zhang¹, Z. Y. Zhang⁶⁷, G. Zhao¹, J. Zhao³¹, J. Y. Zhao^{1,53}, J. Z. Zhao^{1,48}, Lei Zhao^{62,48}, Ling Zhao¹, M. G. Zhao³⁵, Q. Zhao¹, S. J. Zhao⁷⁰, Y. B. Zhao^{1,48}, Y. X. Zhao²⁴, Z. G. Zhao^{62,48}, A. Zhemchugov^{28,a}, B. Zheng⁶³, J. P. Zheng^{1,48}, Y. H. Zheng⁵³, B. Zhong³³, C. Zhong⁶³, L. P. Zhou^{1,53}, Q. Zhou^{1,53}, X. Zhou⁶⁷, X. K. Zhou⁵³, X. R. Zhou^{62,48}, X. Y. Zhou³¹, A. N. Zhu^{1,53}, J. Zhu³⁵, K. Zhu¹, K. J. Zhu^{1,48,53}, S. H. Zhu⁶¹, T. J. Zhu⁶⁸, W. J. Zhu³⁵, W. J. Zhu^{9,f}, Y. C. Zhu^{62,48}, Z. A. Zhu^{1,53}, B. S. Zou¹, J. H. Zou¹

¹ *Institute of High Energy Physics, Beijing 100049, People's Republic of China*

² *Beihang University, Beijing 100191, People's Republic of China*

³ *Beijing Institute of Petrochemical Technology, Beijing 102617, People's Republic of China*

⁴ *Bochum Ruhr-University, D-44780 Bochum, Germany*

⁵ *Carnegie Mellon University, Pittsburgh, Pennsylvania 15213, USA*

⁶ *Central China Normal University, Wuhan 430079, People's Republic of China*

⁷ *China Center of Advanced Science and Technology, Beijing 100190, People's Republic of China*

⁸ *COMSATS University Islamabad, Lahore Campus, Defence Road, Off Raiwind Road, 54000 Lahore, Pakistan*

⁹ *Fudan University, Shanghai 200443, People's Republic of China*

¹⁰ *G.I. Budker Institute of Nuclear Physics SB RAS (BINP), Novosibirsk 630090, Russia*

¹¹ *GSI Helmholtzcentre for Heavy Ion Research GmbH, D-64291 Darmstadt, Germany*

¹² *Guangxi Normal University, Guilin 541004, People's Republic of China*

¹³ *Hangzhou Normal University, Hangzhou 310036, People's Republic of China*

¹⁴ *Helmholtz Institute Mainz, Staudinger Weg 18, D-55099 Mainz, Germany*

¹⁵ *Henan Normal University, Xinxiang 453007, People's Republic of China*

¹⁶ *Henan University of Science and Technology, Luoyang 471003, People's Republic of China*

¹⁷ *Huangshan College, Huangshan 245000, People's Republic of China*

¹⁸ *Hunan Normal University, Changsha 410081, People's Republic of China*

¹⁹ *Hunan University, Changsha 410082, People's Republic of China*

²⁰ *Indian Institute of Technology Madras, Chennai 600036, India*

²¹ *Indiana University, Bloomington, Indiana 47405, USA*

- ²² INFN Laboratori Nazionali di Frascati , (A)INFN Laboratori Nazionali di Frascati, I-00044, Frascati, Italy; (B)INFN Sezione di Perugia, I-06100, Perugia, Italy; (C)University of Perugia, I-06100, Perugia, Italy
- ²³ INFN Sezione di Ferrara, (A)INFN Sezione di Ferrara, I-44122, Ferrara, Italy; (B)University of Ferrara, I-44122, Ferrara, Italy
- ²⁴ Institute of Modern Physics, Lanzhou 730000, People's Republic of China
- ²⁵ Institute of Physics and Technology, Peace Ave. 54B, Ulaanbaatar 13330, Mongolia
- ²⁶ Jilin University, Changchun 130012, People's Republic of China
- ²⁷ Johannes Gutenberg University of Mainz, Johann-Joachim-Becher-Weg 45, D-55099 Mainz, Germany
- ²⁸ Joint Institute for Nuclear Research, 141980 Dubna, Moscow region, Russia
- ²⁹ Justus-Liebig-Universitaet Giessen, II. Physikalisches Institut, Heinrich-Buff-Ring 16, D-35392 Giessen, Germany
- ³⁰ Lanzhou University, Lanzhou 730000, People's Republic of China
- ³¹ Liaoning Normal University, Dalian 116029, People's Republic of China
- ³² Liaoning University, Shenyang 110036, People's Republic of China
- ³³ Nanjing Normal University, Nanjing 210023, People's Republic of China
- ³⁴ Nanjing University, Nanjing 210093, People's Republic of China
- ³⁵ Nankai University, Tianjin 300071, People's Republic of China
- ³⁶ North China Electric Power University, Beijing 102206, People's Republic of China
- ³⁷ Peking University, Beijing 100871, People's Republic of China
- ³⁸ Qufu Normal University, Qufu 273165, People's Republic of China
- ³⁹ Shandong Normal University, Jinan 250014, People's Republic of China
- ⁴⁰ Shandong University, Jinan 250100, People's Republic of China
- ⁴¹ Shanghai Jiao Tong University, Shanghai 200240, People's Republic of China
- ⁴² Shanxi Normal University, Linfen 041004, People's Republic of China
- ⁴³ Shanxi University, Taiyuan 030006, People's Republic of China
- ⁴⁴ Sichuan University, Chengdu 610064, People's Republic of China
- ⁴⁵ Soochow University, Suzhou 215006, People's Republic of China
- ⁴⁶ South China Normal University, Guangzhou 510006, People's Republic of China
- ⁴⁷ Southeast University, Nanjing 211100, People's Republic of China
- ⁴⁸ State Key Laboratory of Particle Detection and Electronics, Beijing 100049, Hefei 230026, People's Republic of China
- ⁴⁹ Sun Yat-Sen University, Guangzhou 510275, People's Republic of China
- ⁵⁰ Suranaree University of Technology, University Avenue 111, Nakhon Ratchasima 30000, Thailand
- ⁵¹ Tsinghua University, Beijing 100084, People's Republic of China
- ⁵² Turkish Accelerator Center Particle Factory Group, (A)Istanbul Bilgi University, HEP Res. Cent., 34060 Eyup, Istanbul, Turkey; (B)Near East University, Nicosia, North Cyprus, Mersin 10, Turkey
- ⁵³ University of Chinese Academy of Sciences, Beijing 100049, People's Republic of China
- ⁵⁴ University of Groningen, NL-9747 AA Groningen, The Netherlands
- ⁵⁵ University of Hawaii, Honolulu, Hawaii 96822, USA

- ⁵⁶ *University of Jinan, Jinan 250022, People's Republic of China*
- ⁵⁷ *University of Manchester, Oxford Road, Manchester, M13 9PL, United Kingdom*
- ⁵⁸ *University of Minnesota, Minneapolis, Minnesota 55455, USA*
- ⁵⁹ *University of Muenster, Wilhelm-Klemm-Str. 9, 48149 Muenster, Germany*
- ⁶⁰ *University of Oxford, Keble Rd, Oxford, UK OX13RH*
- ⁶¹ *University of Science and Technology Liaoning, Anshan 114051, People's Republic of China*
- ⁶² *University of Science and Technology of China, Hefei 230026, People's Republic of China*
- ⁶³ *University of South China, Hengyang 421001, People's Republic of China*
- ⁶⁴ *University of the Punjab, Lahore-54590, Pakistan*
- ⁶⁵ *University of Turin and INFN, (A)University of Turin, I-10125, Turin, Italy; (B)University of Eastern Piedmont, I-15121, Alessandria, Italy; (C)INFN, I-10125, Turin, Italy*
- ⁶⁶ *Uppsala University, Box 516, SE-75120 Uppsala, Sweden*
- ⁶⁷ *Wuhan University, Wuhan 430072, People's Republic of China*
- ⁶⁸ *Xinyang Normal University, Xinyang 464000, People's Republic of China*
- ⁶⁹ *Zhejiang University, Hangzhou 310027, People's Republic of China*
- ⁷⁰ *Zhengzhou University, Zhengzhou 450001, People's Republic of China*
- ^a *Also at the Moscow Institute of Physics and Technology, Moscow 141700, Russia*
- ^b *Also at the Novosibirsk State University, Novosibirsk, 630090, Russia*
- ^c *Also at the NRC "Kurchatov Institute", PNPI, 188300, Gatchina, Russia*
- ^d *Also at Goethe University Frankfurt, 60323 Frankfurt am Main, Germany*
- ^e *Also at Key Laboratory for Particle Physics, Astrophysics and Cosmology, Ministry of Education; Shanghai Key Laboratory for Particle Physics and Cosmology; Institute of Nuclear and Particle Physics, Shanghai 200240, People's Republic of China*
- ^f *Also at Key Laboratory of Nuclear Physics and Ion-beam Application (MOE) and Institute of Modern Physics, Fudan University, Shanghai 200443, People's Republic of China*
- ^g *Also at Harvard University, Department of Physics, Cambridge, MA, 02138, USA*
- ^h *Also at State Key Laboratory of Nuclear Physics and Technology, Peking University, Beijing 100871, People's Republic of China*
- ⁱ *Also at School of Physics and Electronics, Hunan University, Changsha 410082, China*
- ^j *Also at Guangdong Provincial Key Laboratory of Nuclear Science, Institute of Quantum Matter, South China Normal University, Guangzhou 510006, China*
- ^k *Also at Frontiers Science Center for Rare Isotopes, Lanzhou University, Lanzhou 730000, People's Republic of China*
- ^l *Also at Lanzhou Center for Theoretical Physics, Lanzhou University, Lanzhou 730000, People's Republic of China*
- ^m *Currently at Istinye University, 34010 Istanbul, Turkey*

ABSTRACT: Using a data set corresponding to an integrated luminosity of 6.32 fb^{-1} recorded by the BESIII detector at center-of-mass energies between 4.178 and 4.226 GeV, an amplitude analysis of the decay $D_s^+ \rightarrow \pi^+ \pi^0 \pi^0$ is performed, and the relative fractions and phases of different intermediate processes are determined. The absolute branching fraction of the decay $D_s^+ \rightarrow \pi^+ \pi^0 \pi^0$ is measured to be $(0.50 \pm 0.04_{\text{stat}} \pm 0.02_{\text{syst}})\%$. The absolute branching fraction of the intermediate process $D_s^+ \rightarrow f_0(980) \pi^+, f_0(980) \rightarrow \pi^0 \pi^0$ is determined to be $(0.21 \pm 0.03_{\text{stat}} \pm 0.03_{\text{syst}})\%$.

KEYWORDS: BESIII, charm physics, amplitude analysis

Contents

1	Introduction	1
2	Detector and data sets	2
3	Event selection	3
4	Amplitude analysis	4
4.1	Further selections	4
4.2	Fit method	6
4.2.1	Spin factors	7
4.2.2	Blatt-Weisskopf barrier factors	8
4.2.3	Propagator	8
4.3	Fit results	9
4.4	Systematic uncertainties for the amplitude analysis	10
5	Branching fraction measurement	12
6	Summary	16

1 Introduction

The constituent quark model has been very successful in explaining the composition of hadrons in the past few decades. In this model, the observed meson spectrum is described as bound $q\bar{q}$ states grouped into $SU(n)$ flavor multiplets. The nonets of pseudo-scalar, vector and tensor mesons have been well identified. Nevertheless, the identification of the scalar-meson nonet is still ambiguous. Distinguishing scalar mesons from non-resonant background is rather difficult due to their broad widths and non-distinctive angular distribution. There are copious candidates for the $J^{PC} = 0^{++}$ nonets [1]. The case with isospin zero states, e.g. $f_0(500)$, $f_0(980)$, $f_0(1370)$, $f_0(1500)$, and $f_0(1710)$, is the most complicated from both experimental and theoretical points of view. Among them, the $f_0(980)$ meson, as a possible tetraquark candidate [2–4], is particularly interesting and can be studied via the hadronic decays $D_s^+ \rightarrow \pi^+\pi^0\pi^0$, $D_s^+ \rightarrow \pi^+\pi^+\pi^-$ and $D_s^+ \rightarrow K^+K^-\pi^+$. Charge conjugation is implied throughout in this paper. The current published branching fraction (BF) of $D_s^+ \rightarrow f_{0(2)}\pi^+$ from the $D_s^+ \rightarrow \pi^+\pi^+\pi^-$ decays has large discrepancies [1, 5, 6] with that measured from the $D_s^+ \rightarrow K^+K^-\pi^+$ decays. The $f_{0(2)}$ contributions may suffer from the contaminations of $a_0(980) \rightarrow K^+K^-$ or $\rho \rightarrow \pi^+\pi^-$ and the $D_s^+ \rightarrow \pi^+\pi^0\pi^0$ decays offer a cleaner environment due to absence of these contributions.

Furthermore, hadronic D_s^+ decays can be used to probe the interplay of short-distance weak-decay matrix elements and long-distance QCD interactions, and the measured BFs

provide valuable information concerning the amplitudes and phases that induce in decay processes [7–11].

The CLEO Collaboration reported a measurement of absolute BF $\mathcal{B}(D_s^+ \rightarrow \pi^+\pi^0\pi^0) = (0.65 \pm 0.13)\%$ [12], using 600 pb^{-1} of e^+e^- collision data recorded at a center-of-mass energy (\sqrt{s}) of 4.17 GeV. In this analysis, by using 6.32 fb^{-1} of data collected with the BESIII detector ranging from $\sqrt{s} = 4.178 \text{ GeV}$ to $\sqrt{s} = 4.226 \text{ GeV}$, we perform the first amplitude analysis of $D_s^+ \rightarrow \pi^+\pi^0\pi^0$ and a more precise measurement of its absolute BF. The amplitude analysis allows the determination of $\mathcal{B}(D_s^+ \rightarrow f_0(980)\pi^+)$, $\mathcal{B}(D_s^+ \rightarrow f_0(1370)\pi^+)$, and $\mathcal{B}(D_s^+ \rightarrow f_2(1270)\pi^+)$.

2 Detector and data sets

The BESIII detector [13] records symmetric e^+e^- collisions provided by the BEPCII storage ring in the range from $\sqrt{s} = 2.00 \text{ GeV}$ to $\sqrt{s} = 4.95 \text{ GeV}$ [14, 15]. The cylindrical core of the BESIII detector covers 93% of the full solid angle and consists of a helium-based multilayer drift chamber (MDC), a plastic scintillator time-of-flight system (TOF), and a CsI(Tl) electromagnetic calorimeter (EMC), which are all enclosed in a superconducting solenoidal magnet providing a magnetic field of 1.0 T. The solenoid is supported by an octagonal flux-return yoke with resistive plate counter muon identification modules interleaved with steel. The charged-particle momentum resolution at 1 GeV/ c is 0.5%, and the dE/dx resolution is 6% for electrons from Bhabha scattering. The EMC measures photon energies with a resolution of 2.5% (5%) at 1 GeV in the barrel (end cap) region. The time resolution in the TOF barrel region is 68 ps, while that in the end cap region is 110 ps. The end cap TOF system was upgraded in 2015 using multi-gap resistive plate chamber technology, providing a time resolution of 60 ps [16–18].

The data samples used in this analysis are listed in Table 1 [19, 20]. Since the cross section of $D_s^{*\pm}D_s^\mp$ production in e^+e^- annihilation is about a factor of twenty larger than that of $D_s^+D_s^-$ [21], and the D_s^{*+} meson decays to γD_s^+ with a dominant BF of $(93.5 \pm 0.7)\%$ [1], the signal events discussed in this paper are selected from the process $e^+e^- \rightarrow D_s^{*\pm}D_s^\mp \rightarrow \gamma D_s^+D_s^-$.

Table 1. The integrated luminosities (\mathcal{L}_{int}) and the requirements on M_{rec} for various collision energies. The definition of M_{rec} is given in Eq. (3.1). The first and the second uncertainties are statistical and systematic, respectively.

\sqrt{s} (GeV)	\mathcal{L}_{int} (pb^{-1})	M_{rec} (GeV/c^2)
4.178	$3189.0 \pm 0.2 \pm 31.9$	[2.050, 2.180]
4.189	$526.7 \pm 0.1 \pm 2.2$	[2.048, 2.190]
4.199	$526.0 \pm 0.1 \pm 2.1$	[2.046, 2.200]
4.209	$517.1 \pm 0.1 \pm 1.8$	[2.044, 2.210]
4.219	$514.6 \pm 0.1 \pm 1.8$	[2.042, 2.220]
4.226	$1047.3 \pm 0.1 \pm 10.2$	[2.040, 2.220]

Simulated data samples produced with a GEANT4-based [22] Monte Carlo (MC) package, which includes the geometric description of the BESIII detector and the detector response, are used to determine detection efficiencies and to estimate backgrounds. The simulation models the beam energy spread and initial state radiation (ISR) in the e^+e^- annihilations with the generator KKMC [23, 24]. The inclusive MC sample includes the production of open charm processes, the ISR production of vector charmonium(-like) states, and the continuum processes incorporated in KKMC [23, 24]. The known decay modes are modelled with EVTGEN [25, 26] using BFs taken from the Particle Data Group [1], and the remaining unknown charmonium decays are modelled with LUNDCHARM [27, 28]. Final state radiation (FSR) from charged final state particles is incorporated using PHOTOS [29].

3 Event selection

The data samples were collected just above the $D_s^{*\pm}D_s^\mp$ threshold, which allows to extract relatively pure samples for amplitude analysis and measurements of absolute BFs of the hadronic D_s^+ meson decays with a tag method. The tag method has single-tag (ST) and double-tag (DT) candidates. The ST candidates are those D_s^\pm mesons without further requirements on the remaining tracks and EMC showers. The DT candidates are identified by fully reconstructing the $D_s^+D_s^-$ mesons, where one of the D_s^\pm mesons decays into the signal mode $D_s^+ \rightarrow \pi^+\pi^0\pi^0$ and the other to a tag mode. The D_s^\pm mesons are reconstructed through the final state particles, i.e. π^\pm , K^\pm , η , η' , K_S^0 and π^0 , whose selection criteria is discussed below.

For charged tracks not originating from K_S^0 decays, the distance of closest approach to the interaction point is required to be less than 10 cm along the beam direction and less than 1 cm in the plane perpendicular to the beam. Particle identification (PID) for charged tracks combines measurements of the specific ionization energy losses in the MDC (dE/dx) and the flight time in the TOF to form a likelihood $\mathcal{L}(h)$ ($h = K, \pi$) for the hypothesis of being a hadron h . A charged hadron is identified as a kaon if $\mathcal{L}(K)$ is larger than $\mathcal{L}(\pi)$, otherwise it is identified as a pion.

The K_S^0 candidates are reconstructed from two oppositely charged tracks satisfying $|\cos\theta| < 0.93$ and the distance of closest approach along the beam direction must be less than 20 cm. The two charged tracks coming from the K_S^0 are assigned as $\pi^+\pi^-$ without imposing further PID criteria. They are constrained to originate from a common vertex and are required to have an invariant mass within $|M_{\pi^+\pi^-} - m_{K_S^0}| < 12 \text{ MeV}/c^2$, where $m_{K_S^0}$ is the K_S^0 mass taken from PDG [1].

Photon candidates are identified using showers in the EMC. The deposited energy of each shower must be more than 25 MeV in the barrel region ($|\cos\theta| < 0.80$) and more than 50 MeV in the end cap region ($0.86 < |\cos\theta| < 0.92$). The angle between the position of each shower in the EMC and any charged track must be greater than 10 degrees to exclude showers originating from charged tracks. The difference between the EMC time and the event start time is required to be within $[0, 700]$ ns to suppress electronic noise and showers unrelated to the event.

The π^0 (η) candidates are reconstructed through $\pi^0 \rightarrow \gamma\gamma$ ($\eta \rightarrow \gamma\gamma$) decays, with at least one photon in the barrel. The invariant masses of the photon pairs for π^0 and η candidates must be in the ranges $[0.115, 0.150]$ GeV/c^2 and $[0.490, 0.580]$ GeV/c^2 , respectively, which are about three times the resolution of the detector. A kinematic fit that constrains the $\gamma\gamma$ invariant mass to the π^0 or η nominal mass [1] is performed to improve the mass resolution. The χ^2 of the kinematic fit is required to be less than 30. The η' candidates are formed from the $\pi^+\pi^-\eta$ combinations with an invariant mass within a range of $[0.946, 0.970]$ GeV/c^2 .

Seven tag modes are used to reconstruct the tag D_s^- candidate and its mass (M_{tag}) is required to fall within the mass window listed in Table 2. The recoiling mass of the tag D_s^- candidate

$$M_{\text{rec}} = \left(\left(\sqrt{s} - \sqrt{|\vec{p}_{D_s^-}|^2 + m_{D_s^-}^2} \right)^2 - |\vec{p}_{D_s^-}|^2 \right)^{1/2} \quad (3.1)$$

is calculated in the e^+e^- center-of-mass system, where $\vec{p}_{D_s^-}$ is the momentum of the D_s^- candidate in the e^+e^- center-of-mass frame and $m_{D_s^-}$ is the known D_s^- mass [1]. The value of M_{rec} is required to be within the region listed in Table 1.

Table 2. Requirements on M_{tag} for various tag modes.

Tag mode	Mass window (GeV/c^2)
$D_s^- \rightarrow K_S^0 K^-$	[1.948, 1.991]
$D_s^- \rightarrow K^+ K^- \pi^-$	[1.950, 1.986]
$D_s^- \rightarrow K_S^0 K^+ \pi^0$	[1.946, 1.987]
$D_s^- \rightarrow K_S^0 K^- \pi^- \pi^+$	[1.958, 1.980]
$D_s^- \rightarrow K_S^0 K^+ \pi^- \pi^-$	[1.953, 1.983]
$D_s^- \rightarrow \pi^- \eta'$	[1.940, 1.996]
$D_s^- \rightarrow K^- \pi^+ \pi^-$	[1.953, 1.986]

4 Amplitude analysis

4.1 Further selections

The following selection criteria are further applied in order to obtain data samples with high purity for the amplitude analysis. The selection criteria discussed in this section are not used in the BF measurement.

An eight-constraint kinematic fit is performed to select photon from $D_s^{*\pm}$ decays and the best DT candidates assuming D_s^- candidates decaying to one of the tag modes and D_s^+ decaying to the signal mode with two hypotheses: the signal D_s^+ comes from a D_s^{*+} or the tag D_s^- comes from a D_s^{*-} . In this kinematic fit, the total four-momentum is constrained to the initial four-momentum of the e^+e^- system, and the invariant masses of $(\gamma\gamma)_{\pi^0}$, $(\pi^+\pi^-)_{K_S^0}$, tag D_s^- , and $D_s^{*+(-)}$ candidates are constrained to the corresponding known

masses [1]. The best combination is chosen with the minimum χ^2 . After the selection, an additional constraint of the signal $\pi^+\pi^0\pi^0$ invariant mass to the known D_s^+ mass is added and the updated four-momenta of final-state particles from the kinematic fit are used for the amplitude analysis in order to ensure that all candidates fall within the phase-space boundary.

The energy of the transition photon from $D_s^{*+} \rightarrow \gamma D_s^+$ is required to be smaller than 0.18 GeV. The recoiling mass against this photon and the signal D_s^+ is required to fall in the range [1.952, 1.995] GeV/ c^2 . The $D_s^+ \rightarrow \pi^+\pi^0\eta$ decay contributes to the background when $\pi^0\eta$ is misreconstructed as $\pi^0\pi^0$. This background is reduced via an “ η ” veto to reject events which simultaneously satisfy $|M_{\gamma_1\gamma_3} - M_\eta| < 10$ MeV/ c^2 and $|M_{\gamma_2\gamma_4} - M_{\pi^0}| < 20$ MeV/ c^2 , where $M_{\gamma_1\gamma_3}$ and $M_{\gamma_2\gamma_4}$ are the invariant masses of any combinations of the photons used to reconstruct the two π^0 s in the signal decay. There is also background originating from $D^0 \rightarrow K^-\pi^+\pi_1^0$ versus $\bar{D}^0 \rightarrow K^+\pi^-\pi_2^0$ decays, where the π^0 from D^0 is denoted as π_1^0 and that from \bar{D}^0 as π_2^0 . It fakes $D_s^+ \rightarrow \pi^+\pi_1^0\pi_2^0$ versus $D_s^- \rightarrow K^+K^-\pi^-$ ($D_s^- \rightarrow \pi^-\pi_1^0\pi_2^0$ versus $D_s^+ \rightarrow K^+K^-\pi^+$) decays by exchanging K^- and π_2^0 (K^+ and π_1^0). This background is excluded by rejecting events which simultaneously satisfy $|M_{K^-\pi^+\pi_1^0(\pi_2^0)} - m_{D^0}| < 40$ MeV/ c^2 and $|M_{K^+\pi^-\pi_2^0(\pi_1^0)} - m_{D^0}| < 40$ MeV/ c^2 , where m_{D^0} is the known D^0 mass [1]. A $K_S^0 \rightarrow \pi^0\pi^0$ mass veto, $M_{\pi^0\pi^0} \notin (0.458, 0.520)$ GeV/ c^2 , is also applied on the signal D_s^+ to remove the peaking background $D_s^+ \rightarrow K_S^0\pi^+$.

Figure 1 shows the fits to the invariant-mass distributions of the D_s^+ candidates reconstructed in the signal mode, M_{sig} , for the two data samples. The signal is described by a MC-simulated shape convolved with a Gaussian resolution function and the background is described by a simulated shape based on inclusive MC samples. Finally, a mass window [1.925, 1.985] GeV/ c^2 is applied. There are 322 and 250 events retained for the amplitude analysis with purities of $(78.9 \pm 2.3)\%$ and $(75.6 \pm 2.9)\%$ for the data samples at $\sqrt{s} = 4.178$ GeV and 4.189-4.226 GeV, respectively.

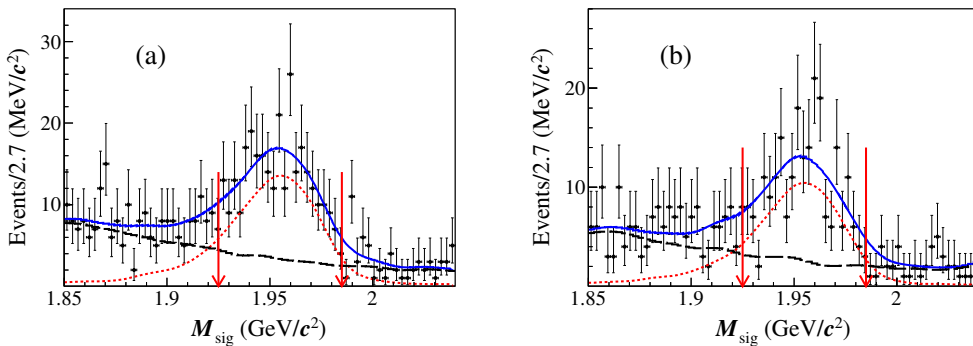


Figure 1. Fits to the M_{sig} distributions of the data samples at $\sqrt{s} =$ (a) 4.178 GeV and (b) 4.189-4.226 GeV. The black points with error bars are data. The blue solid lines are the fit results. The red dotted and the black dashed lines are the fitted signal and background components, respectively. The red arrows indicate the signal regions.

4.2 Fit method

The intermediate-resonant composition is determined by an unbinned maximum-likelihood fit to data. The likelihood function \mathcal{L} is constructed with a signal-background combined probability density function (PDF), which depends on the momenta of the three final state particles:

$$\mathcal{L} = \prod_{i=1}^2 \prod_{k=1}^{N_{D,i}} \left[w^i f_S(p_j^k) + (1 - w^i) f_B(p_j) \right], \quad (4.1)$$

where i and j indicate the data sample groups and the final-state particles, respectively, $N_{D,i}$ is the number of candidate events in the data i , f_S (f_B) is the signal (background) PDF and w is the purity of signal.

The signal PDF is written as

$$f_S(p_j) = \frac{\epsilon(p_j) |\mathcal{A}(p_j)|^2 R_3}{\int \epsilon(p_j) |\mathcal{A}(p_j)|^2 R_3 dp_j}, \quad (4.2)$$

where $\epsilon(p_j)$ is the detection efficiency modeled by a RooNDKeysPdf derived from phase space MC sample, $\mathcal{A}(p_j)$ represents the total amplitude, and R_3 is the standard element of three-body phase space. The isobar formalism is used to model the total amplitude. The total amplitude is the coherent sum of individual amplitudes of intermediate processes, $\mathcal{A} = \sum \rho_n e^{i\phi_n} \mathcal{A}_n$ where magnitude ρ_n and phase ϕ_n are the free parameters to be determined by data. The amplitude of the n^{th} intermediate process (\mathcal{A}_n) is given by

$$\mathcal{A}_n = P_n S_n F_n^r F_n^D, \quad (4.3)$$

where S_n is the spin factor (Sec. 4.2.1); F_n^r and F_n^D are the Blatt-Weisskopf barriers of the intermediate state and the D_s^+ meson, respectively (Sec. 4.2.2); P_n is the propagator of the intermediate resonance (Sec. 4.2.3). The two identical final state π^0 's are symmetrized in the model.

The background PDF is given by

$$f_B(p_j) = \frac{\epsilon(p_j) B_\epsilon(p_j) R_3}{\int \epsilon(p_j) B_\epsilon(p_j) R_3 dp_j}, \quad (4.4)$$

where $B_\epsilon(p_j) = B(p_j)/\epsilon(p_j)$ is the efficiency-corrected background shape. The background events in the signal region from the generic MC sample are used to derive the background shape $B(p_j)$ with RooNDKeysPdf [30]. RooNDKeysPdf is a kernel estimation method [31] implemented in RooFit [30] which models the distribution of an input dataset as a superposition of Gaussian kernels. The $M_{\pi^+\pi^0}$ and $M_{\pi^0\pi^0}$ distributions of events outside the M_{sig} signal region between the data and the generic MC samples are compared to check validity of the background from the generic MC samples. The distributions of background events from the generic MC samples within and outside the M_{sig} signal region are also examined. They are found to be compatible within statistical uncertainties. Note that the $\epsilon(p_j)$ term in Eq. (4.4) is explicitly written out as it is independent of the fitted variables

and is dropped during the log-likelihood fit. The normalization integral terms in the signal and background PDF are handled by MC integration,

$$\int \epsilon(p_j) X(p_j) R_3 dp_j \approx \frac{1}{N_G} \sum_k^{N_M} \frac{X(p_j^k)}{|\mathcal{M}^g(p_j^k)|^2}, \quad (4.5)$$

where $X(p_j)$ is $|\mathcal{A}(p_j)|^2$ or $B_\epsilon(p_j)$, k is the index of the k^{th} event, N_G is the number of the generated MC events and N_M is the number of the selected MC events. The D_s^+ meson in the MC samples used here decays to $\pi^+\pi^0\pi^0$ according to the PDF $\mathcal{M}^g(p_j)$, while the D_s^- meson decays into one of the tag modes. These MC samples are generated with different \sqrt{s} according to the luminosities and cross sections, and satisfy all selection criteria as those of the data samples. At the beginning, a preliminary PDF is used, and then a recursive process is performed until the result converges. To account for any bias caused by differences in PID or tracking efficiencies between data and MC simulation, each signal MC event is weighted with a ratio, $\gamma_\epsilon(p)$, of the efficiency of data to that of MC simulation and the MC integration then becomes

$$\int \epsilon(p_j) X(p_j) R_3 dp_j \approx \frac{1}{N_G} \sum_k^{N_M} \frac{X(p_j^k) \gamma_\epsilon(p_j^k)}{|\mathcal{M}^g(p_j^k)|^2}. \quad (4.6)$$

4.2.1 Spin factors

The spin-projection operators are defined as [32]

$$\begin{aligned} P_{\mu\mu'}^{(1)}(a) &= -g_{\mu\mu'} + \frac{p_{a,\mu} p_{a,\mu'}}{p_a^2}, \\ P_{\mu\nu\mu'\nu'}^{(2)}(a) &= \frac{1}{2} (P_{\mu\mu'}^{(1)}(a) P_{\nu\nu'}^{(1)}(a) + P_{\mu\nu'}^{(1)}(a) P_{\nu\mu'}^{(1)}(a)) \\ &\quad - \frac{1}{3} P_{\mu\nu}^{(1)}(a) P_{\mu'\nu'}^{(1)}(a). \end{aligned} \quad (4.7)$$

The quantities p_a , p_b , and p_c are the momenta of particles a , b , and c , respectively, and $r_a = p_b - p_c$. The covariant tensors are given by

$$\begin{aligned} \tilde{t}_\mu^{(1)}(a) &= -P_{\mu\mu'}^{(1)}(a) r_a^{\mu'}, \\ \tilde{t}_{\mu\nu}^{(2)}(a) &= P_{\mu\nu\mu'\nu'}^{(2)}(a) r_a^{\mu'} r_a^{\nu'}. \end{aligned} \quad (4.8)$$

The spin factors for S , P , and D wave decays are

$$\begin{aligned} S &= 1, & (S \text{ wave}), \\ S &= \tilde{T}^{(1)\mu}(D_s^\pm) \tilde{t}_\mu^{(1)}(a), & (P \text{ wave}), \\ S &= \tilde{T}^{(2)\mu\nu}(D_s^\pm) \tilde{t}_{\mu\nu}^{(2)}(a), & (D \text{ wave}), \end{aligned} \quad (4.9)$$

where the $\tilde{T}^{(l)}$ factors have the same definition as $\tilde{t}^{(l)}$. The tensor describing the D_s^+ decay is denoted by \tilde{T} and that of the a decay is denoted by \tilde{t} .

4.2.2 Blatt-Weisskopf barrier factors

For the process $a \rightarrow bc$, the Blatt-Weisskopf barrier $F_L(p_j)$ [33] is parameterized as a function of the angular momentum L and the momentum q of the final-state particle b or c in the rest system of a ,

$$\begin{aligned} F_{L=0}(q) &= 1, \\ F_{L=1}(q) &= \sqrt{\frac{z_0^2 + 1}{z^2 + 1}}, \\ F_{L=2}(q) &= \sqrt{\frac{z_0^4 + 3z_0^2 + 9}{z^4 + 3z^2 + 9}}, \end{aligned} \quad (4.10)$$

where $z = qR$ and $z_0 = q_0R$. The effective radius of the barrier R is fixed to 3.0 GeV^{-1} for the intermediate resonances and 5.0 GeV^{-1} for the D_s^+ meson.

4.2.3 Propagator

The intermediate resonances $f_2(1270)$ and $f_0(1370)$ are parameterized as relativistic Breit-Wigner functions,

$$P = \frac{1}{(m_0^2 - s_a) - im_0\Gamma(s_a)}, \quad \Gamma(s_a) = \Gamma_0 \left(\frac{q}{q_0}\right)^{2L+1} \left(\frac{m_0}{s_a}\right) \left(\frac{F_L(q)}{F_L(q_0)}\right)^2, \quad (4.11)$$

where s_a denotes the invariant-mass squared of the two final-state particles considered; m_0 and Γ_0 are the mass and the width of the intermediate resonance, respectively, and are fixed to the PDG values [1].

The $f_0(980)$ resonance is represented by the Flatté formula [34],

$$P_{f_0(980)} = \frac{1}{m_{f_0(980)}^2 - s_{\pi^0\pi^0} - i(g_1\rho_{\pi\pi}(s_{\pi^0\pi^0}) + g_2\rho_{K\bar{K}}(s_{\pi^0\pi^0}))}, \quad (4.12)$$

where $s_{\pi^0\pi^0}$ is the $\pi^0\pi^0$ invariant-mass squared and $g_{1,2}$ are coupling constants to the corresponding final states. The parameters are fixed to $g_1 = 0.165 \text{ GeV}/c^2$, $g_2/g_1 = 4.21$ and $m_{f_0(980)} = 955 \text{ MeV}/c^2$, as reported in Ref. [34]. The Lorentz invariant phase-space factors $\rho_{\pi\pi}(s)$ and $\rho_{K\bar{K}}(s)$ are given by

$$\begin{aligned} \rho_{\pi\pi} &= \frac{2}{3} \sqrt{1 - \frac{4m_{\pi^\pm}^2}{s}} + \frac{1}{3} \sqrt{1 - \frac{4m_{\pi^0}^2}{s}}, \\ \rho_{K\bar{K}} &= \frac{1}{2} \sqrt{1 - \frac{4m_{K^\pm}^2}{s}} + \frac{1}{2} \sqrt{1 - \frac{4m_{K^0}^2}{s}}, \end{aligned} \quad (4.13)$$

where m_{π^\pm} , m_{π^0} , m_{K^\pm} , and m_{K^0} are the known masses of π^\pm , π^0 , K^\pm , and K^0 , respectively [1]. The $f_0(500)$ resonance is also an amplitude candidate, and is described by a relativistic Breit-Wigner function or the Bugg lineshape [35].

4.3 Fit results

The Dalitz plot of $M_{\pi^+\pi^0}^2$ versus $M_{\pi^+\pi^0}^2$ for the data samples is shown in Fig. 2(a) and that for the signal MC samples generated based on the results of the amplitude analysis is shown in Fig. 2(b). In the fit, the magnitude and phase of the reference amplitude $D_s^+ \rightarrow f_0(980)\pi^+$ are fixed to 1.0 and 0.0, respectively, while those of other amplitudes are left floating. The masses and widths of all resonances are fixed to the corresponding PDG averages [1], and w^i are fixed to the purities discussed in Sec. 4.1. The systematic uncertainties associated with these fixed parameters are considered by repeating the fit after variation of the fixed parameters according to their uncertainties.

Besides the dominant amplitudes $D_s^+ \rightarrow f_0(980)\pi^+$, $D_s^+ \rightarrow f_0(1370)\pi^+$, and $D_s^+ \rightarrow f_2(1270)\pi^+$, we have tested all possible intermediate resonances including $\rho(1450)$, $f_0(1500)$, $\rho(1700)$, $(\pi\pi)_S$, $(\pi\pi)_P$, $(\pi\pi)_D$ etc., where the subscript denotes a relative S (P or D) wave between final-state particles. We have also examined all possible combinations of these intermediate resonances to check their significances, correlations, and interferences. By requiring a significance larger than 3σ , eventually, $D_s^+ \rightarrow f_0(980)\pi^+$, $D_s^+ \rightarrow f_0(1370)\pi^+$, $D_s^+ \rightarrow f_2(1270)\pi^+$, $D_s^+ \rightarrow \pi^+(\pi^0\pi^0)_D$, and $D_s^+ \rightarrow (\pi^+\pi^0)_D\pi^0$ are chosen for the nominal set. Note that $D_s^+ \rightarrow f_0(500)\pi^+$ is tested but it has a significance less than 2σ .

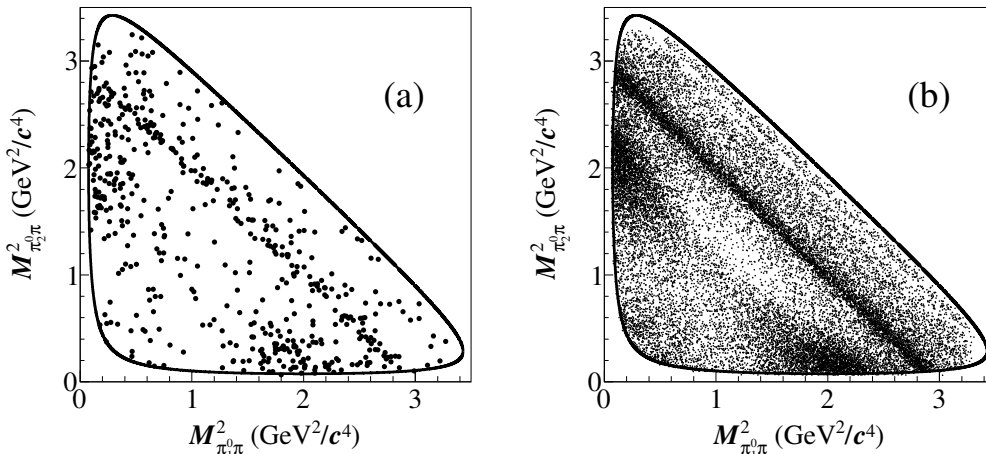


Figure 2. The Dalitz plot of $M_{\pi^+\pi^0}^2$ versus $M_{\pi^+\pi^0}^2$ for (a) the data sample and (b) the signal MC sample generated based on the results of the amplitude analysis at $\sqrt{s} = 4.178\text{--}4.226$ GeV, symmetrized for the indistinguishable π^0 's.

In the calculation of fit fractions (FFs) for individual amplitudes, the phase-space MC truth information is involved with neither detector acceptance nor resolution. The FF for the n^{th} amplitude is defined as

$$\text{FF}_n = \frac{\sum^{N_{\text{gen}}} |c_n \mathcal{A}_n|^2}{\sum^{N_{\text{gen}}} |\mathcal{A}|^2}, \quad (4.14)$$

where N_{gen} is the number of the phase-space MC events at generator level. Interference

between the n^{th} and the n'^{th} amplitudes (IN) is defined as (for $n < n'$ only)

$$\text{IN}_{nn'} = \frac{\sum^{N_{\text{gen}}} 2\text{Re}[c_n c_{n'}^* \mathcal{A}_n \mathcal{A}_{n'}^*]}{\sum^{N_{\text{gen}}} |\mathcal{A}|^2}. \quad (4.15)$$

The statistical fluctuations of FFs are obtained by randomly sampling the fit variables according to their fitted values and covariance matrix. The distribution of each FF is fitted with a Gaussian function and the width of the Gaussian function is defined as the statistical uncertainty of the FF.

The phases, FFs, and statistical significances for the amplitudes are listed in Table 3. The interferences between amplitudes are listed in Table 4. The Dalitz plot projections are shown in Fig. 3. The sum of the FFs is not unity due to interferences between amplitudes. Other tested amplitudes, but not included in the nominal fit, and their significances are listed in Table 5.

Table 3. The phases, FFs, and statistical significances for the amplitudes. The first and second uncertainties in the phases and FFs are statistical and systematic, respectively. The total FF is 111.4%.

Amplitude	Phase ϕ_n (rad)	FF (%)	Significance (σ)
$D_s^+ \rightarrow f_0(980)\pi^+$	0.0(fixed)	$42.0 \pm 4.9 \pm 6.6$	>10
$D_s^+ \rightarrow f_0(1370)\pi^+$	$-0.7 \pm 0.2 \pm 0.3$	$25.8 \pm 4.4 \pm 4.8$	>10
$D_s^+ \rightarrow f_2(1270)\pi^+$	$-0.9 \pm 0.3 \pm 0.3$	$15.0 \pm 4.6 \pm 5.2$	5.0
$D_s^+ \rightarrow \pi^+(\pi^0\pi^0)_D$	$-4.4 \pm 0.2 \pm 0.3$	$19.1 \pm 5.2 \pm 5.2$	6.3
$D_s^+ \rightarrow (\pi^+\pi^0)_D\pi^0$	$-2.3 \pm 0.2 \pm 0.5$	$9.5 \pm 3.4 \pm 5.1$	3.4

Table 4. Interference fraction (%) between amplitudes where the uncertainties are statistical only.

	$f_0(1370)\pi^+$	$f_2(1270)\pi^+$	$\pi^+(\pi^0\pi^0)_D$	$(\pi^+\pi^0)_D\pi^0$
$f_0(980)\pi^+$	-2.6 ± 7.3	0.0 ± 0.1	-0.1 ± 0.1	4.1 ± 2.4
$f_0(1370)\pi^+$		-0.1 ± 0.1	0.0 ± 0.1	9.2 ± 1.8
$f_2(1270)\pi^+$			-15.7 ± 4.4	-3.3 ± 1.7
$\pi^+(\pi^0\pi^0)_D$				-4.6 ± 2.8

4.4 Systematic uncertainties for the amplitude analysis

The systematic uncertainties for the amplitude analysis are summarized in Table 6, with their definitions described below:

- i Resonant parameters. The masses and the widths of $f_0(1370)$ and $f_2(1270)$ are varied by their corresponding uncertainties [1]. The mass and coupling constants of the $f_0(980)$ Flatté formula are varied according to Ref. [34]. The changes of the phases ϕ and FFs are assigned as the associated systematic uncertainties.

Table 5. Significances of amplitudes tested, but not included in the nominal fit.

Amplitude	Significance (σ)
$D_s^+ \rightarrow f_0(500)\pi^+$	1.5
$D_s^+ \rightarrow f_0(1500)\pi^+$	2.1
$D_s^+ \rightarrow \rho(1450)^+\pi^0$	2.4
$D_s^+ \rightarrow \rho^+\pi^0$	2.0
$D_s^+ \rightarrow (\pi^+\pi^0)_P\pi^0$	1.5
$D_s^+ \rightarrow \pi^+(\pi^0\pi^0)_S$	1.3

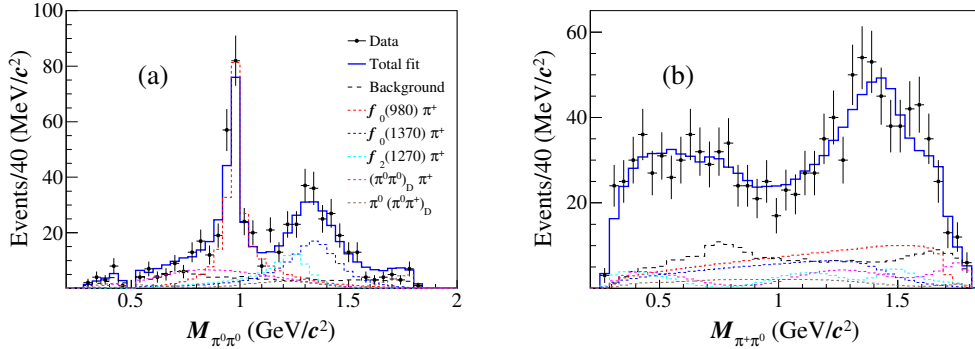


Figure 3. The projections of (a) $M_{\pi^0\pi^0}$ and (b) $M_{\pi^+\pi^0}$ from the nominal fit. Two $M_{\pi^+\pi^0}$ are calculated and added due to the indistinguishable π^0 's. The data samples are represented by points with error bars, the fit results by the solid blue lines, and the background estimated from inclusive MC samples by the black dashed lines. Colored dashed lines show the components of the fit model. Due to interference effects, the total is not necessarily equal to the sum of the components.

- ii R values. The associated systematic uncertainties are estimated by repeating the fit procedure by varying the radii of the intermediate state and D_s^+ mesons within 1 GeV^{-1} .
- iii Background estimation. First, the purities of signals for the two sample groups, i.e. w in Eq. (4.1) are varied by their corresponding statistical uncertainties to study uncertainties associated with backgrounds. The differences caused by the variation are assigned as the uncertainties. Second, an alternative MC-simulated shape is used to examine the uncertainty arising from the background shape modeling. Alternative background shapes are extracted with the relative fractions of the dominant backgrounds from $e^+e^- \rightarrow q\bar{q}$ and non- $D_s^{*\pm}D_s^\mp$ open-charm processes varied by the statistical uncertainties of their cross sections.
- iv Resonances with significances less than 3σ . The corresponding uncertainties are taken to be the differences of the phases ϕ and FFs with and without the intermediate resonances with statistical significances less than 3σ .

Table 6. Systematic uncertainties on the phase ϕ and FF for each amplitude in unit of the corresponding statistical uncertainty. The sources are: (i) fixed parameters in the amplitudes, (ii) the R values, (iii) background, (iv) resonances with significances less than 3σ .

Amplitude		Source				Total
		i	ii	iii	iv	
$D_s^+ \rightarrow f_0(980)\pi^+$	FF	1.07	0.29	0.31	0.70	1.35
$D_s^+ \rightarrow f_0(1370)\pi^+$	ϕ	1.32	0.30	0.34	0.42	1.46
	FF	1.06	0.20	0.09	0.08	1.09
$D_s^+ \rightarrow f_2(1270)\pi^+$	ϕ	0.56	0.09	0.23	0.85	1.05
	FF	0.93	0.53	0.36	0.16	1.14
$D_s^+ \rightarrow \pi^+(\pi^0\pi^0)_D$	ϕ	0.56	0.42	0.24	1.53	1.70
	FF	0.88	0.46	0.10	0.11	1.00
$D_s^+ \rightarrow (\pi^+\pi^0)_D\pi^0$	ϕ	1.36	0.09	0.17	2.15	2.55
	FF	0.72	0.14	0.20	1.30	1.50

v Experimental effects. To estimate the systematic uncertainty related to the difference between MC simulation and data associated with the PID and tracking efficiencies, γ_ϵ in Eq. (4.6), the amplitude fit is performed varying the PID and tracking efficiencies according to their uncertainties. The differences from the nominal results are so tiny that this source of systematic uncertainty is negligible.

5 Branching fraction measurement

In addition to the selection criteria for final-state particles described in Sec. 3, it is required that π^+ must have momentum greater than 100 MeV/ c to remove soft π^+ from D^{*+} decays. The best tag candidate with M_{rec} closest to the D_s^{*+} known mass [1] is chosen if there are multiple ST candidates. The data sets are organized into three sample groups, 4.178 GeV, 4.189-4.219 GeV, and 4.226 GeV, that were acquired during the same year under consistent running conditions.

The yields for various tag modes are obtained by fitting the corresponding M_{tag} distributions and listed in Table 7. As an example, the fits to the M_{tag} spectra of the ST candidates in the data sample at $\sqrt{s} = 4.178$ GeV are shown in Fig. 4. In the fits, the signal is modeled by a MC-simulated shape convolved with a Gaussian function to take into account the data-MC resolution difference. The background is described by a second-order Chebyshev function. MC studies show that there is no significant peaking background in any tag mode, except for $D^- \rightarrow K_S^0\pi^-$ and $D_s^- \rightarrow \eta\pi^+\pi^-\pi^-$ faking the $D_s^- \rightarrow K_S^0K^-$ and $D_s^- \rightarrow \pi^-\eta'$ tags, respectively. Therefore, the MC-simulated shapes of these two peaking background sources are added to the background models.

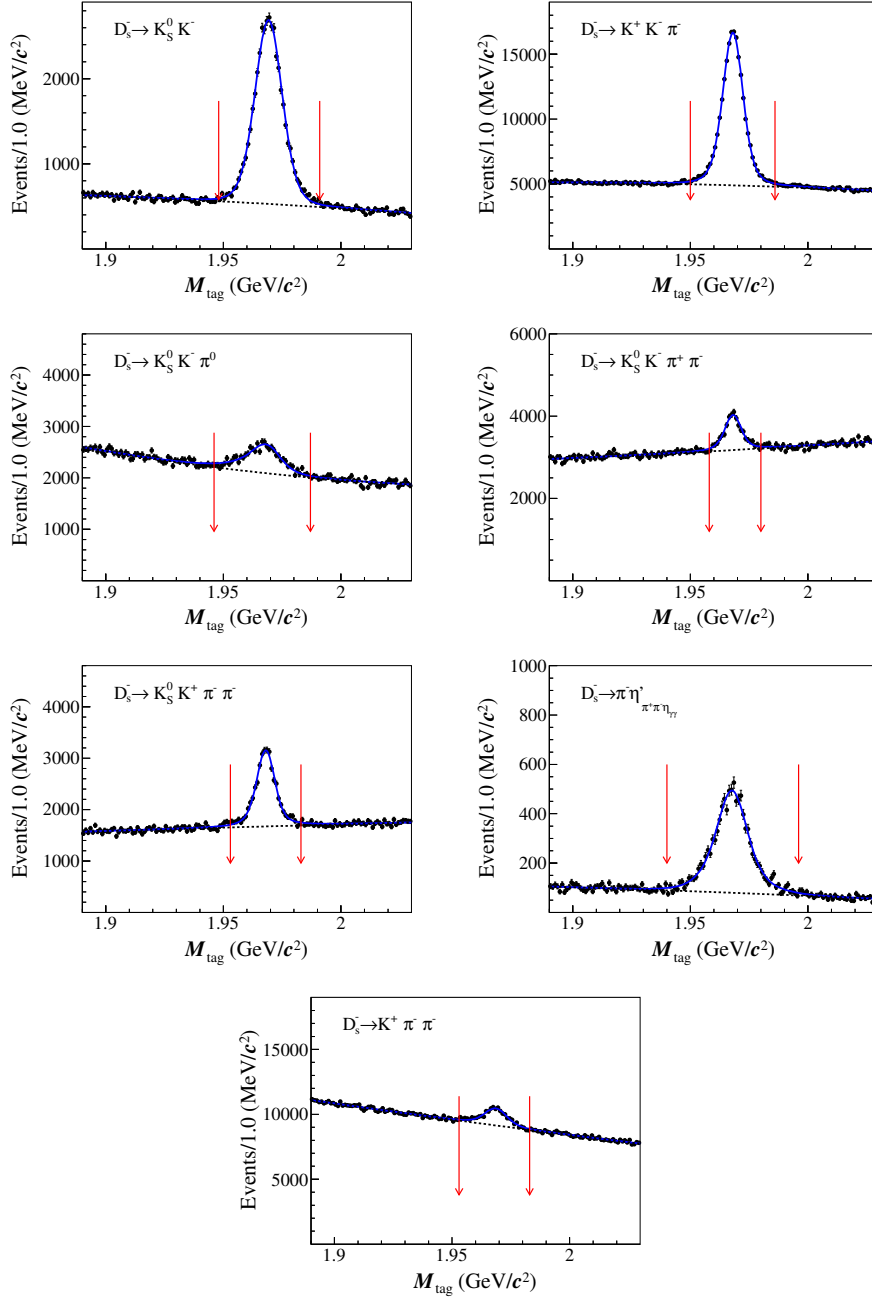


Figure 4. Fits to the M_{tag} distributions of the ST candidates from the data sample at $\sqrt{s} = 4.178$ GeV. The points with error bars are data, the blue solid lines are the total fits, and the black dashed lines are background. The pairs of red arrows denote the signal regions.

Table 7. The ST yields for the samples collected at $\sqrt{s} =$ (I) 4.178 GeV, (II) 4.199-4.219 GeV, and (III) 4.226 GeV. The uncertainties are statistical.

Tag mode	(I) N_{ST}	(II) N_{ST}	(III) N_{ST}
$D_s^- \rightarrow K_S^0 K^-$	31941 ± 312	18559 ± 261	6582 ± 160
$D_s^- \rightarrow K^+ K^- \pi^-$	137240 ± 614	81286 ± 505	28439 ± 327
$D_s^- \rightarrow K_S^0 K^- \pi^0$	11385 ± 529	6832 ± 457	2227 ± 220
$D_s^- \rightarrow K_S^0 K^- \pi^- \pi^+$	8093 ± 326	5269 ± 282	1662 ± 217
$D_s^- \rightarrow K_S^0 K^+ \pi^- \pi^-$	15719 ± 289	8948 ± 231	3263 ± 172
$D_s^- \rightarrow \pi^- \eta'$	7759 ± 141	4428 ± 111	1648 ± 74
$D_s^- \rightarrow K^- \pi^+ \pi^-$	17423 ± 666	10175 ± 448	4984 ± 458
Total	229560 ± 1186	135497 ± 937	48805 ± 688

Once a tag mode is identified, the signal decay $D_s^+ \rightarrow \pi^+ \pi^0 \pi^0$ is searched for at the recoiling side. In the case of multiple candidates, the DT candidate with the average mass, $(M_{\text{sig}} + M_{\text{tag}})/2$, closest to the D_s^+ nominal mass is retained. A $K_S^0 \rightarrow \pi^0 \pi^0$ mass veto, $M_{\pi^0 \pi^0} \notin (0.458, 0.520)$ GeV/ c^2 , is applied on the signal D_s^+ to remove the peaking background $D_s^+ \rightarrow K_S^0 \pi^+$.

To measure the BF, we start from the following equations for each tag mode:

$$N_{\text{tag}}^{\text{ST}} = 2N_{D_s^+ D_s^-} \mathcal{B}_{\text{tag}} \epsilon_{\text{tag}}^{\text{ST}}, \quad (5.1)$$

$$N_{\text{tag, sig}}^{\text{DT}} = 2N_{D_s^+ D_s^-} \mathcal{B}_{\text{tag}} \mathcal{B}_{\text{sig}} \epsilon_{\text{tag, sig}}^{\text{DT}}, \quad (5.2)$$

where $N_{D_s^+ D_s^-}$ is the total number of $D_s^{*\pm} D_s^\mp$ pairs produced from the $e^+ e^-$ collisions; $N_{\text{tag}}^{\text{ST}}$ is the ST yield for the tag mode; $N_{\text{tag, sig}}^{\text{DT}}$ is the DT yield; \mathcal{B}_{tag} and \mathcal{B}_{sig} are the BFs of the tag and signal modes, respectively; $\epsilon_{\text{tag}}^{\text{ST}}$ is the ST efficiency to reconstruct the tag mode; and $\epsilon_{\text{tag, sig}}^{\text{DT}}$ is the DT efficiency to reconstruct both the tag and the signal decay modes. In the case of more than one tag modes and sample groups,

$$N_{\text{total}}^{\text{DT}} = \sum_{\alpha, i} N_{\alpha, \text{sig}, i}^{\text{DT}} = \mathcal{B}_{\text{sig}} \sum_{\alpha, i} 2N_{D_s^+ D_s^-} \mathcal{B}_{\alpha} \epsilon_{\alpha, \text{sig}, i}^{\text{DT}}, \quad (5.3)$$

where α represents tag modes in the i^{th} sample group. By isolating \mathcal{B}_{sig} , we find

$$\mathcal{B}_{\text{sig}} = \frac{N_{\text{total}}^{\text{DT}}}{\mathcal{B}_{\pi^0 \rightarrow \gamma\gamma}^2 \sum_{\alpha, i} N_{\alpha, i}^{\text{ST}} \epsilon_{\alpha, \text{sig}, i}^{\text{DT}} / \epsilon_{\alpha, i}^{\text{ST}}}, \quad (5.4)$$

where $N_{\alpha, i}^{\text{ST}}$ and $\epsilon_{\alpha, i}^{\text{ST}}$ are obtained from the data and inclusive MC samples, respectively. $\epsilon_{\alpha, \text{sig}, i}^{\text{DT}}$ is determined with signal MC samples with $D_s^+ \rightarrow \pi^+ \pi^0 \pi^0$ events are generated according to the results of the amplitude analysis. The BF for $\pi^0 \rightarrow \gamma\gamma$ is introduced to account for the fact that the signal is reconstructed through this decay.

The DT yield $N_{\text{total}}^{\text{DT}}$ is found to be 587 ± 44 from the fit to the M_{sig} distribution of the selected $D_s^+ \rightarrow \pi^+ \pi^0 \pi^0$ candidates. The fit result is shown in Fig. 5, where the signal shape is described by a MC-simulated shape convolved with a Gaussian function to

take into account the data-MC resolution difference. The background is described by a simulated shape from the inclusive MC sample. A small peaking background originating from $D^0 \rightarrow K^- \pi^+ \pi^0$ is considered in the inclusive MC sample. Taking the difference in π^0 reconstruction efficiencies for each signal mode between data and MC simulation into account by multiplying the efficiencies by a factor of 99.5% for each π^0 , we determine the BF of $D_s^+ \rightarrow \pi^+ \pi^0 \pi^0$ to be $(0.50 \pm 0.04_{\text{stat}} \pm 0.02_{\text{syst}})\%$.

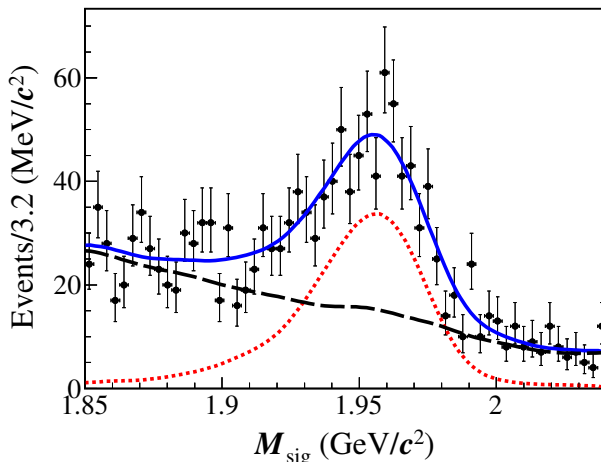


Figure 5. Fit to the M_{sig} distribution of the DT candidates from the data samples at $\sqrt{s} = 4.178\text{--}4.226$ GeV. The data are represented by points with error bars, the total fit by the blue solid line, and the fitted signal and the fitted background by the red dotted and the black dashed lines, respectively.

The relative systematic uncertainty for the total yield of the ST D_s^- mesons is assigned to be 0.4% by examining the changes of the fit yields when varying the signal shape, background shape, and taking into account the background fluctuation in the fit. The systematic uncertainty due to the signal shape is studied by repeating the fit without the convolved Gaussian. The MC-simulated background shape is altered by varying the relative fractions of the dominant backgrounds from $e^+e^- \rightarrow q\bar{q}$ or non- $D_s^{*+}D_s^-$ open-charm processes by their statistical uncertainties of their related cross sections. The largest change is taken as the corresponding systematic uncertainty. The π^+ tracking (PID) efficiency is studied with the processes $e^+e^- \rightarrow K^+K^-\pi^+\pi^-$ ($e^+e^- \rightarrow K^+K^-\pi^+\pi^-(\pi^0)$ and $\pi^+\pi^-\pi^+\pi^-(\pi^0)$). The systematic uncertainty due to tracking (PID) efficiency is estimated to be 1%(1%). The systematic uncertainty of the π^0 reconstruction efficiency is investigated by using a control sample of the process $e^+e^- \rightarrow K^+K^-\pi^+\pi^-\pi^0$. The selection criteria listed in Sec. 3 are used to reconstruct the two kaons and the two pions. The recoiling mass distribution of $K^+K^-\pi^+\pi^-$ is fitted to obtain the total number of π^0 's and the π^0 selection is applied to determine the number of reconstructed π^0 's. The average ratio between data and MC efficiencies of π^0 reconstruction, weighted by the corresponding momentum spectra, is estimated to be 0.995 ± 0.008 . After correcting the simulated efficiencies to data by this ratio, the residual uncertainty 0.8% is assigned as the systematic uncertainty arising from

each π^0 reconstruction. The uncertainty due to the limited MC statistics is obtained by $\sqrt{\sum_i (f_i \frac{\delta \epsilon_i}{\epsilon_i})^2}$, where f_i is the tag yield fraction, and ϵ_i and $\delta \epsilon_i$ are the signal efficiency and the corresponding uncertainty of tag mode i , respectively. The uncertainty from the amplitude analysis model is estimated by varying the model parameters based on their error matrix. The distribution of 600 efficiencies resulting from this variation is fitted by a Gaussian function and the fitted width divided by the mean value is taken as a relative uncertainty. All of the systematic uncertainties are summarized in Table 8. Adding them in quadrature gives a total systematic uncertainty in the BF measurement of 4.0%.

Table 8. Systematic uncertainties relative to the central value in the BF measurement.

Source	Systematic uncertainty (%)
D_s^- yield	0.4
Signal shape	1.6
Background shape	2.8
π^+ PID efficiency	1.0
π^+ tracking efficiency	1.0
π^0 reconstruction	1.6
MC statistics	0.2
Signal MC model	0.9
Total	4.0

6 Summary

An amplitude analysis of the decay $D_s^+ \rightarrow \pi^+ \pi^0 \pi^0$ has been performed for the first time. Amplitudes with significances larger than 3σ were selected. The results for the FFs and phases of the different intermediate processes are listed in Table 3. With the detection efficiency calculated according to the intermediate processes found in the amplitude analysis, the BF for the decay $D_s^+ \rightarrow \pi^+ \pi^0 \pi^0$ is measured to be $(0.50 \pm 0.04_{\text{stat}} \pm 0.02_{\text{syst}})\%$. The precision is improved by about a factor of two compared to the PDG value [1] due to the large dataset collected with the BESIII detector. The BFs for the intermediate processes are calculated with $\mathcal{B}_i = \text{FF}_i \times \mathcal{B}(D_s^+ \rightarrow \pi^+ \pi^0 \pi^0)$ and listed in Table 9. The BF of $D_s^+ \rightarrow f_0(980)\pi^+$ with $f_0(980) \rightarrow \pi^0 \pi^0$ is measured for the first time. In addition, no significant signal of $f_0(500)$ is observed. Assuming the BF ratio between $f_{0(2)} \rightarrow \pi^+ \pi^-$ and $f_{0(2)} \rightarrow \pi^0 \pi^0$ to be 2 based on isospin symmetry, our results favors with those from $D_s^+ \rightarrow \pi^+ \pi^+ \pi^-$ than from $D_s^+ \rightarrow K^+ K^- \pi^+$.

Acknowledgments

The BESIII collaboration thanks the staff of BEPCII and the IHEP computing center for their strong support. This work is supported in part by National Key R&D Program of

Table 9. The BFs for intermediate processes. The first and the second uncertainties are statistical and systematic, respectively.

Intermediate process	BF (10^{-3})
$D_s^+ \rightarrow f_0(980)\pi^+, f_0(980) \rightarrow \pi^0\pi^0$	$2.1 \pm 0.3 \pm 0.3$
$D_s^+ \rightarrow f_0(1370)\pi^+, f_0(1370) \rightarrow \pi^0\pi^0$	$1.3 \pm 0.2 \pm 0.2$
$D_s^+ \rightarrow f_2(1270)\pi^+, f_2(1270) \rightarrow \pi^0\pi^0$	$0.8 \pm 0.3 \pm 0.3$
$D_s^+ \rightarrow \pi^+(\pi^0\pi^0)_D$	$1.0 \pm 0.3 \pm 0.3$
$D_s^+ \rightarrow (\pi^+\pi^0)_D\pi^0$	$0.5 \pm 0.2 \pm 0.3$

China under Contracts Nos. 2020YFA0406400, 2020YFA0406300; National Natural Science Foundation of China (NSFC) under Contracts Nos. 11625523, 11635010, 11735014, 11822506, 11835012, 11875054, 11935015, 11935016, 11935018, 11961141012, 12022510, 12025502, 12035009, 12035013, 12061131003; the Chinese Academy of Sciences (CAS) Large-Scale Scientific Facility Program; Joint Large-Scale Scientific Facility Funds of the NSFC and CAS under Contracts Nos. U2032104, U1732263, U1832207; CAS Key Research Program of Frontier Sciences under Contract No. QYZDJ-SSW-SLH040; 100 Talents Program of CAS; INPAC and Shanghai Key Laboratory for Particle Physics and Cosmology; ERC under Contract No. 758462; European Union Horizon 2020 research and innovation programme under Contract No. Marie Skłodowska-Curie grant agreement No 894790; German Research Foundation DFG under Contracts Nos. 443159800, Collaborative Research Center CRC 1044, FOR 2359, FOR 2359, GRK 214; Istituto Nazionale di Fisica Nucleare, Italy; Ministry of Development of Turkey under Contract No. DPT2006K-120470; National Science and Technology fund; Olle Engkvist Foundation under Contract No. 200-0605; STFC (United Kingdom); The Knut and Alice Wallenberg Foundation (Sweden) under Contract No. 2016.0157; The Royal Society, UK under Contracts Nos. DH140054, DH160214; The Swedish Research Council; U. S. Department of Energy under Contracts Nos. DE-FG02-05ER41374, DE-SC-0012069.

References

- [1] PARTICLE DATA GROUP collaboration, *Review of Particle Physics*, [*PTEP* **2020** \(2020\) 083C01](#).
- [2] J. Weinstein and N. Isgur, $qq\bar{q}\bar{q}$ system in a potential model, [*Phys. Rev. D* **27** \(1983\) 588](#).
- [3] J. Weinstein and N. Isgur, $K\bar{K}$ molecules, [*Phys. Rev. D* **41** \(1990\) 2236](#).
- [4] X. D. Cheng, H. B. Li, B. Wei, Y. G. Xu and M. Z. Yang, *Study of $D \rightarrow a_0(980)e^+\nu_e$ decay in the light-cone sum rules approach*, [*Phys. Rev. D* **96** \(2017\) 033002](#).
- [5] E687 collaboration, *Analysis of the $D^+, D_s^+ \rightarrow \pi^-\pi^+\pi^+$ Dalitz plots*, [*Phys. Lett. B* **407** \(1997\) 79](#).
- [6] E791 collaboration, *Study of the $D_s^+ \rightarrow \pi^-\pi^+\pi^+$ decay and measurement of f_0 masses and widths*, [*Phys. Rev. Lett.* **86** \(2001\) 765 \[hep-ex/0007027\]](#).

- [7] H. B. Li and X. R. Lyu, *Study of the Standard Model with weak decays charmed hadrons*, *arXiv hep-ex* (2021) 00908 [[hep-ex/00908](#)].
- [8] Y. K. Hsiao, Y. Yu and B. C. Ke, *Resonant $a_0(980)$ state in triangle rescattering $D_s^+ \rightarrow \pi^+\pi^0\eta$ decays*, *Eur. Phys. J. C* **80** (2020) 895.
- [9] B. Bhattacharya and J. L. Rosner, *Decays of charmed mesons to PV final states*, *Phys. Rev. D* **79** (2009) 034016.
- [10] H. Y. Cheng and C. W. Chiang, *Two-body hadronic charmed meson decays*, *Phys. Rev. D* **81** (2010) 074021.
- [11] F. S. Yu, X. X. Wang and C. D. Lü, *Nonleptonic two-body decays of charmed mesons*, *Phys. Rev. D* **84** (2011) 074019.
- [12] CLEO collaboration, *Measurement of the pseudoscalar decay constant f_{D_s} using $D_s^+ \rightarrow \tau^+\nu$, $\tau^+ \rightarrow \rho^+\bar{\nu}$ decays*, *Phys. Rev. D* **80** (2009) 112004.
- [13] M. Ablikim, Z. An, J. Bai, N. Berger, J. Bian, X. Cai et al., *Design and construction of the BESIII detector*, *Nucl. Instrum. Meth. A* **614** (2010) 345.
- [14] C. Yu et al., *BEPCII Performance and Beam Dynamics Studies on Luminosity*, in *Proc. of International Particle Accelerator Conference (IPAC'16), Busan, Korea, May 8-13, 2016*, no. 7 in International Particle Accelerator Conference, (Geneva, Switzerland), pp. 1014–1018, JACoW, June, 2016, [DOI](#).
- [15] BESIII collaboration, *Future physics programme of BESIII*, *Chin. Phys. C* **44** (2020) 040001.
- [16] X. Li, Y. Sun, C. Li, Z. Liu, Y. Heng, M. Shao et al., *Study of MRPC technology for BESIII endcap-TOF upgrade*, *Radiat. Detect. Technol. Methods* **1** (2017) 13.
- [17] Y. X. Guo, S. S. Sun, F. F. An, R. X. Yang, M. Zhou, Z. Wu et al., *The study of time calibration for upgraded end cap TOF of BESIII*, *Radiat. Detect. Technol. Methods* **1** (2017) 15.
- [18] P. Cao, H. Chen, M. Chen, H. Dai, Y. Heng, X. Ji et al., *Design and construction of the new BESIII endcap time-of-flight system with mrpc technology*, *Nucl. Instrum. Meth. A* **953** (2020) 163053.
- [19] BESIII collaboration, *Measurement of the center-of-mass energies at BESIII via the di-muon process*, *Chin. Phys. C* **40** (2016) 063001.
- [20] BESIII collaboration, *Precision measurement of the integrated luminosity of the data taken by BESIII at center of mass energies between 3.810 GeV and 4.600 GeV*, *Chin. Phys. C* **39** (2015) 093001.
- [21] CLEO collaboration, *Measurement of charm production cross sections in e^+e^- annihilation at energies between 3.97 and 4.26 GeV*, *Phys. Rev. D* **80** (2009) 072001.
- [22] GEANT4 collaboration, *GEANT4 – a simulation toolkit*, *Nucl. Instrum. Meth. A* **506** (2003) 250.
- [23] S. Jadach, B. F. L. Ward and Z. Wař, *Coherent exclusive exponentiation for precision Monte Carlo calculations*, *Phys. Rev. D* **63** (2001) 113009.
- [24] S. Jadach, B. F. L. Ward and Z. Wař, *The precision Monte Carlo event generator KK for two-fermion final states in e^+e^- collisions*, *Computer Physics Communications* **130** (2000) 260.

- [25] D. Lange, *The EvtGen particle decay simulation package*, *Nucl. Instrum. Meth. A* **462** (2001) 152.
- [26] R. G. Ping, *Event generators at BESIII*, *Chin. Phys. C* **32** (2008) 599.
- [27] J. C. Chen, G. S. Huang, X. R. Qi, D. H. Zhang and Y. S. Zhu, *Event generator for J/ψ and $\psi(2S)$ decay*, *Phys. Rev. D* **62** (2000) 034003.
- [28] R. L. Yang, R. G. Ping and H. Chen, *Tuning and validation of the Lundcharm model with J/ψ decays*, *Chin. Phys. Lett.* **31** (2014) 061301.
- [29] E. Richter-Was, *QED bremsstrahlung in semileptonic B and leptonic τ decays*, *Phys. Lett. B* **303** (1993) 163.
- [30] W. Verkerke and D. P. Kirkby, *RooFit Users Manual v2.07*. 2006.
- [31] K. Cranmer, *Kernel estimation in high-energy physics*, *Computer Physics Communications* **136** (2001) 198.
- [32] B. S. Zou and D.V. Bugg, *Covariant tensor formalism for partial-wave analyses of ψ decay to mesons*, *Eur. Phys. J. A* **16** (2003) 537.
- [33] BABAR collaboration, *Dalitz plot analysis of $D_s^+ \rightarrow K^+K^-\pi^+$* , *Phys. Rev. D* **83** (2011) 052001.
- [34] BESIII collaboration, *Resonances in $J/\psi \rightarrow \phi\pi^+\pi^-$ and ϕK^+K^-* , *Phys. Lett. B* **607** (2005) 243.
- [35] D. V. Bugg, *The mass of the σ pole*, *Journal of Physics G: Nuclear and Particle Physics* **34** (2006) 151.